










RESEARCH ARTICLE | JUNE 20 2023

Microwave backscatter enhancement using radial anisotropy in biomimetic core-shell spheres

Special Collection: [Fundamentals and Applications of Metamaterials: Breaking the Limits](#)

Ewan D. Finlayson ; Cameron P. Gallagher ; Thomas Whittaker ; Athanasios Goulas ; Daniel S. Engstrøm ; William Whittow ; J. Roy Sambles ; Alastair P. Hibbins ; Alexander W. Powell 

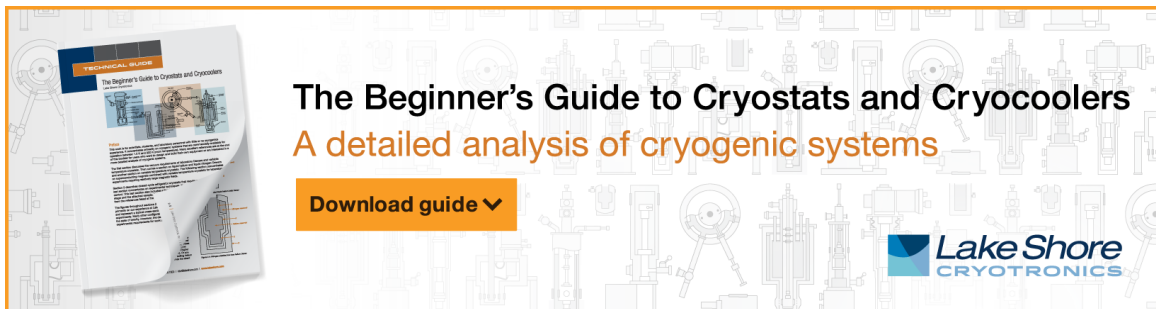


Appl. Phys. Lett. 122, 251701 (2023)

<https://doi.org/10.1063/5.0152735>




CrossMark



The Beginner's Guide to Cryostats and Cryocoolers
A detailed analysis of cryogenic systems

[Download guide](#)



Microwave backscatter enhancement using radial anisotropy in biomimetic core-shell spheres

Cite as: Appl. Phys. Lett. **122**, 251701 (2023); doi: [10.1063/5.0152735](https://doi.org/10.1063/5.0152735)

Submitted: 31 March 2023 · Accepted: 5 June 2023 ·

Published Online: 20 June 2023



View Online



Export Citation



CrossMark

Ewan D. Finlayson,^{1,2,a)} Cameron P. Gallagher,¹ Thomas Whittaker,² Athanasios Goulas,²
Daniel S. Engstrøm,² William Whittow,² J. Roy Sambles,¹ Alastair P. Hibbins,¹
and Alexander W. Powell^{1,a)}

AFFILIATIONS

¹Department of Physics and Astronomy, University of Exeter, Exeter EX4 4QL, United Kingdom

²Wolfson School of Mechanical, Electrical and Manufacturing Engineering, Loughborough University, Loughborough LE11 3TU, United Kingdom

Note: This paper is part of the APL Special Collection on Fundamentals and Applications of Metamaterials: Breaking the Limits.

^{a)}Authors to whom correspondence should be addressed: e.finlayson@exeter.ac.uk and a.w.powell@exeter.ac.uk

ABSTRACT

Enhanced backscattering of microwave radiation is demonstrated experimentally in a biomimetic radially anisotropic spherical metamaterial component. The core-shell device replicates the optical function of nanospheres observed in the tapetum reflector of the compound eye of the shrimp *Litopenaeus vannamei* (Boone, 1931) and translates the effect from the optical domain to microwave frequencies. Analytical Mie theory calculations and numerical-method simulations are used to describe the origin of the observed scattering from a single dielectric sphere in terms of its multipolar Mie resonances. The fabrication of components using additive manufacture and their experimental characterization are described. The results show that the introduction of radial anisotropy in the shell more than doubles the monostatic radar cross section compared to the equivalent isotropic case. This work represents a practical demonstration of a synthetic bio-inspired structure, harnessing performance-enhancing adaptations that have evolved in nature. The results augment the range of techniques available for the control of electromagnetic scattering with relevance to applications in the manipulation of radar return signals.

© 2023 Author(s). All article content, except where otherwise noted, is licensed under a Creative Commons Attribution (CC BY) license (<http://creativecommons.org/licenses/by/4.0/>). <https://doi.org/10.1063/5.0152735>

Electromagnetic metamaterials are engineered composites that are typically composed of constituents with sub-wavelength dimensions. They can be designed to have tailored or enhanced electromagnetic properties and can even exhibit material parameters that are not found in nature. The ability to realize the often complex geometries required has been enhanced by advances in fabrication techniques such as 3D printing and nanofabrication. Moreover, the natural world itself provides instructive examples that inform electromagnetics research through the many elaborate structures that have evolved in living organisms for the control of light.¹ Natural structures that determine optical properties, including reflectivity, iridescence, and polarization control, have provided inspiration and design information for analogous biomimetic devices² as well as the translation of their geometries from optical to microwave length scales.³ One goal for engineered metamaterials and meta-atoms is the manipulation of the scattering of electromagnetic waves by particles with dimensions smaller than or close to the wavelength. It has been shown that the

strength and directionality of scattering may be controlled by structuring a particle in order to adjust the frequencies and magnitudes of the Mie resonances that it supports.⁴ The term “superscattering” is used to refer to total scattering from multiple resonances that exceeds the theoretical limit for that of a single resonance.⁵ Diverse applications have been identified for tailoring of scattering, including wireless power transfer, radar signature control, and the enhancement of nonlinear optical processes,^{4,6,7} while mode selection and tuning are used in the design of dielectric resonance antennas.^{8,9}

An important concept arising from the spectral coincidence or “stacking” of multiple Mie resonances is termed the first Kerker condition,¹⁰ as illustrated in Fig. 1.¹¹ In this case, the electric dipole (ED) and magnetic dipole (MD) scatter the incident field with the same phase in the forward direction and opposite phase in the backward direction. If the magnitudes of the two modes are matched, the consequent wave interference eliminates backscatter and enhances forward scattering. For modes arising from a dielectric particle, the contrasting

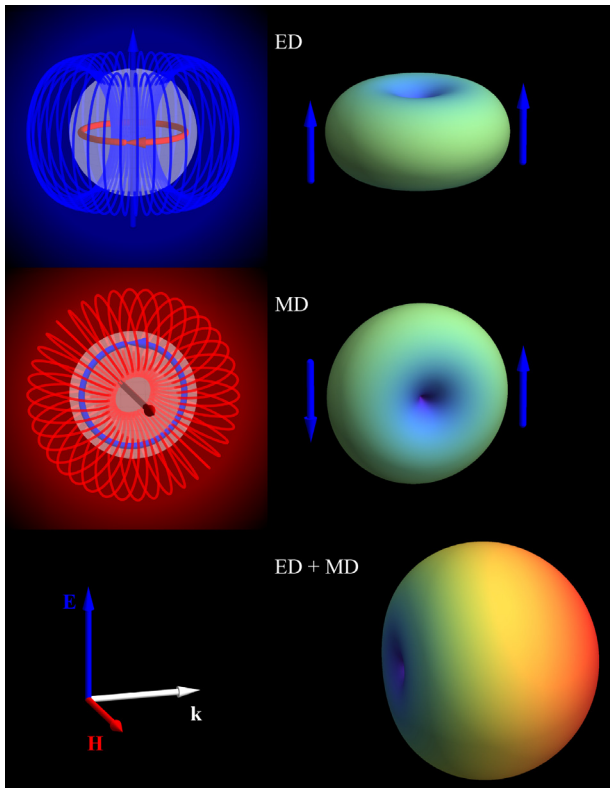


FIG. 1. Sketch illustrating Mie scattering and the first Kerker condition. (Left) Indicative electromagnetic near-fields of the electric dipole (ED) and magnetic dipole (MD) resonances for a generic dielectric sphere with size comparable to the wavelength. (Right) The corresponding radiation patterns with equal electric field amplitude specified for each mode, and their sum that has zero backscatter. Arrows indicate the relative polarity of the electric fields in the forward and backward directions.

electric field distributions between the electric and magnetic mode families within the particle allows their resonances to be tuned differentially through structuring of the internal geometry. For example, the introduction of a low permittivity core within a high permittivity sphere was proposed in order to preferentially move the spectral positions of the electric modes to higher frequencies due to their greater electric field flux at the center of the sphere.¹² The enhancement of backscattering was then demonstrated by using this effect to pull electric modes into overlap with selected magnetic modes having the requisite relative phase.¹³ Among other geometries and concepts that have been considered theoretically, the example of homogeneous radially anisotropic spheres has relevance to this work.^{14,15}

In recent years, researchers have identified materials and nanostructures that use optical scattering to enhance the sensitivity of compound eyes of certain shrimp species. The presence of the crystalline pteridine material isoxanthopterin was identified,¹⁶ and its anisotropic refractive index was found to have the value $n = 1.96$ for one of its principal axes. This very high index among biological materials suggests utility of isoxanthopterin in optical reflectors. The arrangement of isoxanthopterin crystals in spherical core-shell nanoparticles was characterized as featuring a radially anisotropic shell surrounding an

isotropic core¹⁷ and was identified as providing efficient backscattering. The role of the scattering in enhancing the sensitivity of the compound eyes was reported, whereby the presence of particles in a retinal structure called the tapetum reflector helps to concentrate light in the light-sensitive rhabdoms of the retina as well as reducing crosstalk between adjacent rhabdoms. Beck *et al.* described the influence of the high refractive index for light polarized tangentially to the particle surface on the magnitude of the scattering cross section due to the alignment of the electric fields of the magnetic modes.¹⁸ Short range ordering of the nanoparticles has also been reported to contribute to the light gathering.¹⁹

In this work, we demonstrate a functional biomimetic component for microwave backscatter enhancement inspired by the shrimp eye structures. The component harnesses an advantageous physical configuration arrived at through evolution and showcases the use of additive manufacture to realize a microwave version requiring a complex geometry. Experimental results and simulations are presented for design variants that elucidate the role of the anisotropy in manipulating the backscatter, while providing a quantitative indication of the performance benefit introduced vs equivalent structures without anisotropy. The work is motivated by the desire to increase the palette of techniques available for the manipulation of electromagnetic radiation.

In order to replicate the biological scattering structure and investigate the physical origin of the backscattering enhancement, a suite of simulations was undertaken leading to the design and fabrication of a set of experimental microwave samples. Three different structures were specified with permittivities that are summarized in Table I. These core-shell structures are illustrated in Fig. 2. The first design was based on the particle found in the eye of the whiteleg shrimp *L. vannamei* described by Palmer *et al.*,¹⁷ which featured a radially birefringent shell with ordinary refractive index (tangential polarization) $n_o = 1.96$, extraordinary index (radial polarization) $n_e = 1.40$, an isotropic cytoplasm core with refractive index 1.33 and radius $r = 95$ nm, a shell thickness $t = 70$ nm, and an overall diameter of 330 nm. The shell region had a spatial-average refractive index $n_{av} = 1.77$, using the definition

$$n_{av} = (2n_o + n_e)/3. \quad (1)$$

While this structure yielded backscatter in the wavelength range 350–700 nm, our version is scaled and translated for operation in the microwave domain. It is noted that the characterization of the shell of the shrimp-eye structure found a layered assembly of birefringent isoxanthopterin platelets. Such a configuration is distinguished from the microwave version presented here, in which the construction is entirely of isotropic component materials. The effective birefringence of the shell region instead results from the electromagnetic boundary

TABLE I. Effective relative permittivities specified for the core and shell regions of the three sample designs.

	Design 1	Design 2	Design 3
Core	2.0	2.0	2.0
Shell	3.85 (tangential) 1.89 (radial)	3.12 (isotropic)	4.5 (isotropic)

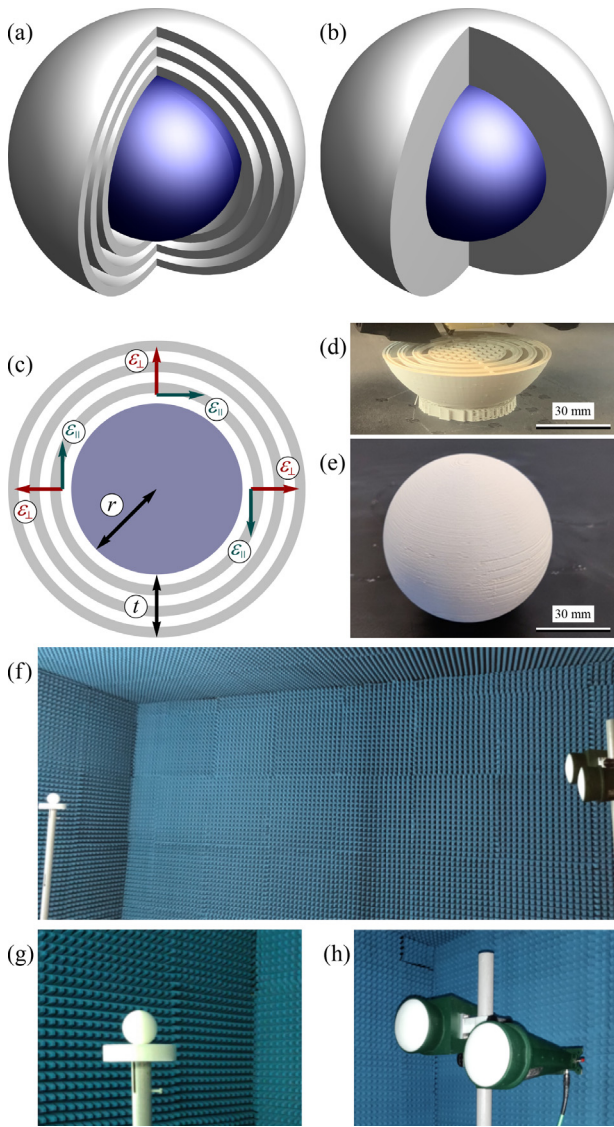


FIG. 2. Core-shell sample geometries and experimental setup. (a)–(c) Partial sections of core-shell particles, indicating the core region (blue) and the solid layers of the shell (grey). (a) Geometry featuring a radially anisotropic shell formed from concentric layers of isotropic material and air as implemented in design 1. (b) Variant geometry featuring a solid isotropic shell, as used for designs 2 and 3. (c) Cross section schematic showing the local orientation of radially anisotropic principal axes. (d) Anisotropic sample during 3D printing. (e) The completed sample, with diameter 66 mm. (f)–(h) Experimental setup for microwave backscattering measurements. (f) General view of the setup within the anechoic chamber. (g) Detail of the sample and its mount. (h) Detail of the horn antennas. A metal screen (not shown) was placed vertically between the antennas to reduce crosstalk between them.

conditions at the interfaces between successive layers with contrasting permittivity. Specifically, the continuity of the tangential electric field \mathbf{E} and the normal (i.e., radial) electric displacement \mathbf{D} must be satisfied. The consequent “form birefringence” has principal axes that are orientated tangentially and radially with respect to the particle. For a

plane wave propagating in an “effective medium” comprising an infinite array of alternating flat layers, the effective permittivities are given by²⁰

$$\epsilon_{\perp} = \frac{\epsilon_1 \epsilon_2}{f_1 \epsilon_2 + f_2 \epsilon_1}, \quad \epsilon_{\parallel} = f_1 \epsilon_1 + f_2 \epsilon_2, \quad (2)$$

where f_1 and f_2 are the fractional thicknesses of the two layers and ϵ_1 and ϵ_2 are their respective relative permittivities. The multi-layered shell yields radial anisotropy in the permittivity using these principles in a modified form in which the sub-wavelength stratification is applied to a spherical geometry and only has a small number of boundaries. Accordingly, the target relative permittivity for the anisotropic shell constituents was $\epsilon_r = 6.6$ for the solid layers with air spacer layers and a core permittivity of $\epsilon_r = 2.0$.

For comparison with the anisotropic shrimp-eye replica, two designs were specified with shells that were isotropic both in terms of the materials of their construction as well as omitting form anisotropy. Design 2 featured a shell permittivity of $\epsilon_r = 3.12$, thereby providing an isotropic equivalent to the anisotropic sample according to Eq. (1). The purpose of this design was to investigate the difference in scattering behavior depending on the presence or absence of anisotropy in the shell. In a third design, the permittivity of the isotropic shell was tailored in order to obtain an approximate match in the backscattering magnitude and spectrum to that of the shrimp-eye analogue. The purpose of this experiment was to identify the increase in isotropic permittivity required to realize the same performance offered by a lower index anisotropic medium. All three designs featured an overall diameter of 66 mm, comprising a core of radius $r = 19$ mm and a shell of thickness $t = 14$ mm. The anisotropic shell was formed from six layers, each 2.33 mm-thick, alternating between solid dielectric and air.

Numerical simulations of the electromagnetic scattering behavior of the full structures were performed for plane wave incidence using the finite-element method in the Comsol Multiphysics software.²¹ An analytical Mie theory calculation method^{11,15} was used to obtain the scattering contributions from individual Mie resonances. In the analytical model, the concentrically layered shell was replaced by a homogeneous anisotropic medium according to the effective medium calculations, and the air spacer layers were estimated to have an ϵ_r of 1.1 owing to the presence of sparse, thin (0.6 mm) solid struts. The designs were prepared using the assumption of lossless materials. The samples were fabricated by fused-filament fabrication additive manufacturing using a Raise3D Pro2 (Raise3D, Irvine US). In each sample, the core was printed with a sub-wavelength lattice leaving air gaps with an infill fraction that was tuned to achieve the specified isotropic relative permittivity. The required infill fraction was calculated according to an effective medium calculation,²²

$$v = \frac{\epsilon_{\text{reff}} - 1}{\epsilon_{ro} - 1}, \quad (3)$$

in which v is the volume fraction of solid material, ϵ_r is the desired relative permittivity, and ϵ_{ro} is the relative permittivity of bulk material. The parameters were verified by a set of calibration tests, which were measured using a 5.1 GHz split-post dielectric resonator (SPDR), (QWED, Warsaw, Poland) yielding the effective relative permittivity ϵ_{eff} and effective loss tangent $\tan \delta_{\text{eff}}$. The anisotropic design was printed entirely with PREPERM ABS800 (Premix Oy, Rajamäki, Finland) dielectric thermoplastic ($\epsilon_r = 8$, $\tan \delta = 3.3 \times 10^{-3}$), with a

core infill percentage of 23% ($\epsilon_{eff} = 2.0251$, $\tan \delta_{eff} = 1.59 \times 10^{-3}$). Each solid layer of the shell region was printed with an infill of 90% ($\epsilon_{eff} = 6.6548$, $\tan \delta_{eff} = 3.16 \times 10^{-3}$). Both isotropic designs were printed using multiple materials, and their dielectric parameters were obtained from measurements on 3D printed test samples. The cores were printed using high-impact polystyrene (HIPS) (BASF, Germany) (measured $\epsilon_r = 2.49$, $\tan \delta = 8.53 \times 10^{-4}$), with an infill density of 70% (calculated $\epsilon_{eff} = 2.043$, $\tan \delta_{eff} = 7.277 \times 10^{-4}$). The solid shells of both isotropic designs were printed with PREPERM ABS320 ($\epsilon_{eff} = 3.07$, $\tan \delta_{eff} = 4.066 \times 10^{-3}$) and PREPERM ABS175-TP20280 ($\epsilon_{eff} = 4.43$, $\tan \delta_{eff} = 3.676 \times 10^{-3}$), respectively. All parts were printed using 0.800 mm brass nozzles, a layer thickness of 0.200 mm, a printing speed of 40 mm/s, and extrusion and build surface temperatures of 240 °C and 100 °C, respectively. A 20% overlap between the contour and the infill sections was applied to improve part density.

The frequency-dependent backscattering from the microwave samples was measured using a quasi-monostatic configuration in an anechoic chamber, as shown in Fig. 3. The transmission and collection of radiation were performed by a pair of Flann Microwave DP240-AB dual-polarized horn antennas, which were approximately co-located, connected to an Anritsu MS46122B vector network analyzer. The sample was mounted on a fiberglass pole topped with Rohacell 31HF foam, which has a low relative permittivity ($\epsilon_r = 1.04$). The horns were positioned 3 m from the sample in order to present approximately flat incident phase fronts across its spatial extent. The measurements were calibrated using a 50 mm-diameter stainless steel sphere.

In this section, results are first presented for designs 1 and 2, comparing the anisotropic shrimp-eye analogue with its isotropic equivalent with shell permittivity $\epsilon_r = 3.12$. Design 3 is discussed later in the context of the effect of the use of materials with larger permittivity. The simulations and experimental results for the monostatic radar cross section (RCS), normalized to the cross-sectional area, for designs 1 and 2 are shown in Fig. 3. The experimental data [Fig. 3(b)] show quantitative agreement with the finite-element method simulations [Fig. 3(a)]. The comparison between the designs shows that the introduction of anisotropy results in an RCS enhancement of more than a factor of two for the lowest frequency scattering peak at around 3 GHz. A small downward shift in frequency is also observed. An alternative measure of backscatter is presented in finite-element simulations in the supplementary material, whereby the normalized backscatter is integrated over the backward hemisphere [Fig. S1(b)] and is compared with the total normalized scattering cross section [Fig. S1(a)]. This measure shows a similar backscatter enhancement to the monostatic RCS results. The hemispherical backscattering accounts for approximately one quarter of the total scattering in the anisotropic design at frequencies near the lowest frequency RCS peak.

Figures 3(c) and 3(d) show analytical Mie theory calculations for the same two designs of the scattering cross section (σ_{sca}) contributions, normalized to the sample cross-sectional area, within the frequency range of interest due to the first three modes of each of the electric and magnetic resonance families: dipoles, quadrupoles, and octupoles. Of particular note are the relative strengths of the electric dipole (ED) and magnetic dipole (MD) modes. The simulations show that neither of the designs have a match in the ED and MD strengths within the 2–3 GHz frequency range in which the relevant RCS peak occurs. Accordingly, they do not satisfy the first Kerker condition for total backscatter suppression. However, the results show that the

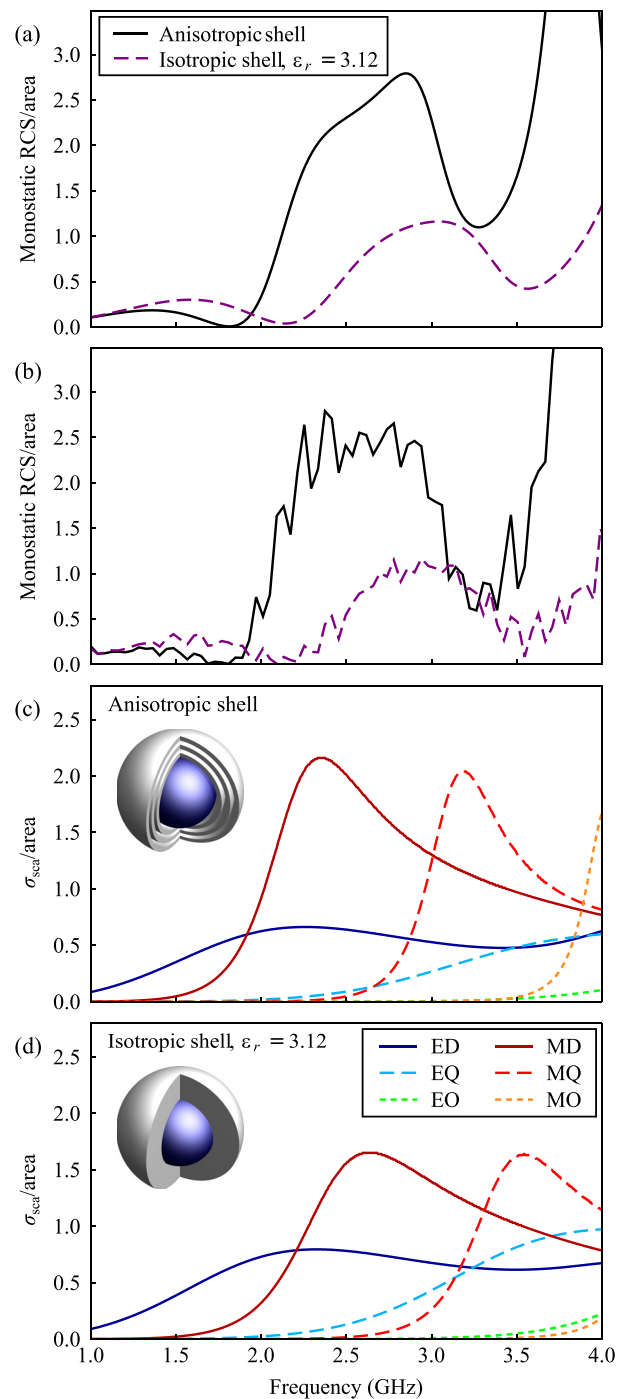


FIG. 3. Scattering performance of the anisotropic sample (design 1) and its isotropic equivalent (design 2). (a) and (b) Monostatic radar cross section normalized to the sample cross-sectional area, (a) Finite-element method simulations. (b) Experimental measurements. (c) and (d) Analytical Mie theory calculations of the scattering cross section contributions due to the first three modes of each of the electric (E) and magnetic (M) resonance families. Labels D, Q, and O refer to dipoles, quadrupoles, and octupoles, respectively. (c) Anisotropic shell (design 1). (d) Isotropic shell, $\epsilon_r = 3.12$ (design 2).

design with radial anisotropy in the shell has a strengthened MD resonance relative to that of the isotropic design, while leaving the ED strength largely unaffected. For the isotropic component [Fig. 3(d)], the dimensionless scattering parameter for the MD mode has a peak value of 1.65 at 2.64 GHz, which is a factor of 2.06 stronger than the broad ED resonance that peaks at 2.32 GHz. For the anisotropic design [Fig. 3(c)], the MD parameter reaches 2.16 at 2.35 GHz, a factor of 3.27 stronger than the approximately coincident ED mode.

Observing the effect of introducing anisotropy on the backscattered radiation highlights the importance of the difference between the internal field geometries of the two mode families as well as their relation to the orientation of the principal axes of the shell permittivity. The electric dipole has no radial magnetic field component, while the magnetic dipole has no radial electric field.¹¹ The strengthening of the MD magnitude is, therefore, expected due to the alignment of its electric fields with the large tangential permittivity, while the electric fields of the ED mode are polarized orthogonally to that direction. By altering the relative strength of the electric and magnetic resonances in this way, the scattering performance is pulled further from the first Kerker condition by the weakening of the destructive interference in the backward direction. Consequently, the backscatter is enhanced. The observed downward shift in frequency may also be attributed to the larger tangential permittivity, which results in the resonance occurring at a longer wavelength.

The results presented above indicate that the presence of anisotropy provides an advantage in biological optical structures, where the available dielectric material parameters are constrained. Greater flexibility is available in the microwave domain in terms of permittivity, which allows one to investigate what isotropic shell permittivity is required to achieve equivalent backscattering performance to the anisotropic case. Figure 4(a) shows finite-element method simulations of monostatic RCS and corresponding experimental measurements in the absence of anisotropy for a sample with a shell permittivity of $\epsilon_r = 4.5$ (design 3). The results are comparable to that of the anisotropic sample; however, the permittivity corresponds to a refractive index of 2.12, which is larger than is typically found in biological materials.^{17,23,24} Figure 4(b) shows simulations of the scattering cross sections for the modes of this design with shell permittivity $\epsilon_r = 4.5$. In this case, the MD scattering parameter reaches 2.63 at 2.15 GHz, a factor of 2.18 stronger than the ED mode. While the magnitude of all of the modes is increased relative to those of the lower permittivity version shown in Fig. 3(d), the relative strengths of the ED and MD modes remain similar. Therefore, an increase in RCS is expected as a consequence of an increase in total scattering. Simulations of the backscatter integrated over the backward hemisphere [supplementary material, Fig. S2(b)] show comparable magnitude with the anisotropic design, while the total normalized scattering cross section [Fig. S2(a)] shows increased scattering at the relevant frequencies. These results demonstrate the utility of the inclusion of anisotropy as a strategy for scattering enhancement in the shrimp eye.

Advances in additive manufacturing techniques have expanded the range of dielectric materials that they offer for microwave applications. The available material properties include larger relative permittivities than those discussed above,²⁵ leading to further scope to manipulate the resonances using the same multilayered shell design concept. The consequence of increasing the permittivity of the solid layers in the shell of our anisotropic architecture is illustrated in

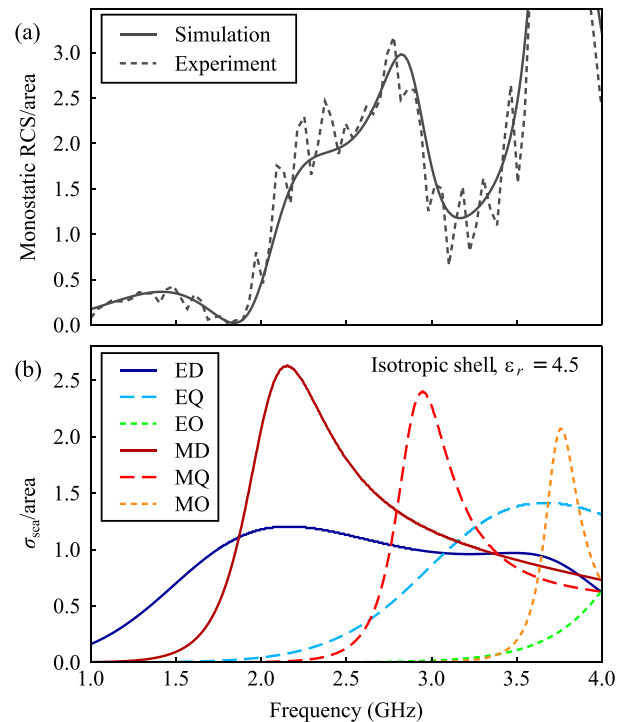


FIG. 4. Scattering performance of the isotropic sample with an elevated shell permittivity $\epsilon_r = 4.5$ (design 3). (a) Monostatic radar cross sections normalized to cross-sectional area. Comparison of finite-element method simulation and experimental measurement. (b) Analytical Mie theory calculations of the scattering cross section contributions due to the first three modes of each of the electric (E) and magnetic (M) resonance families.

analytical method calculations in Fig. 5. The scattering cross section contributions from the first five multipoles of each mode family are compared for electric modes [Fig. 5(a)] and magnetic modes [Fig. 5(b)]. The monostatic RCS is shown in Fig. 5(c). The effective anisotropy parameter $\epsilon_{\parallel} - \epsilon_{\perp}$ is displayed on the primary ordinate axis. The isotropic permittivity of the solid layers of the shell required to obtain this anisotropy, as calculated using Eqs. (2), is shown on the secondary ordinate axis. Its magnitude covers the range 5–30, while all other design parameters are unchanged from the shrimp-eye analogue design. Each plot is normalized to the cross-sectional area of the design. The results show that the spectral positions of the electric and magnetic modes move down in frequency at differing rates as the anisotropy is increased. For larger anisotropies, the ED and MD modes can be separated in frequency, thus further preventing destructive interference in the backward direction at frequencies approaching 1 GHz. This mechanism complements the tuning of the relative strengths of the modes. Furthermore, the potential for stacking higher-order multipoles to achieve a superscattering effect²⁶ is apparent, although beyond the scope of this work. Through these mechanisms, the concentrically layered shell concept offers a plurality of processes for mode manipulation and scattering control, over and above that suggested by the nanoparticle found in the shrimp eye.

In conclusion, we have designed, fabricated, and experimentally demonstrated a metamaterial component that provides enhanced

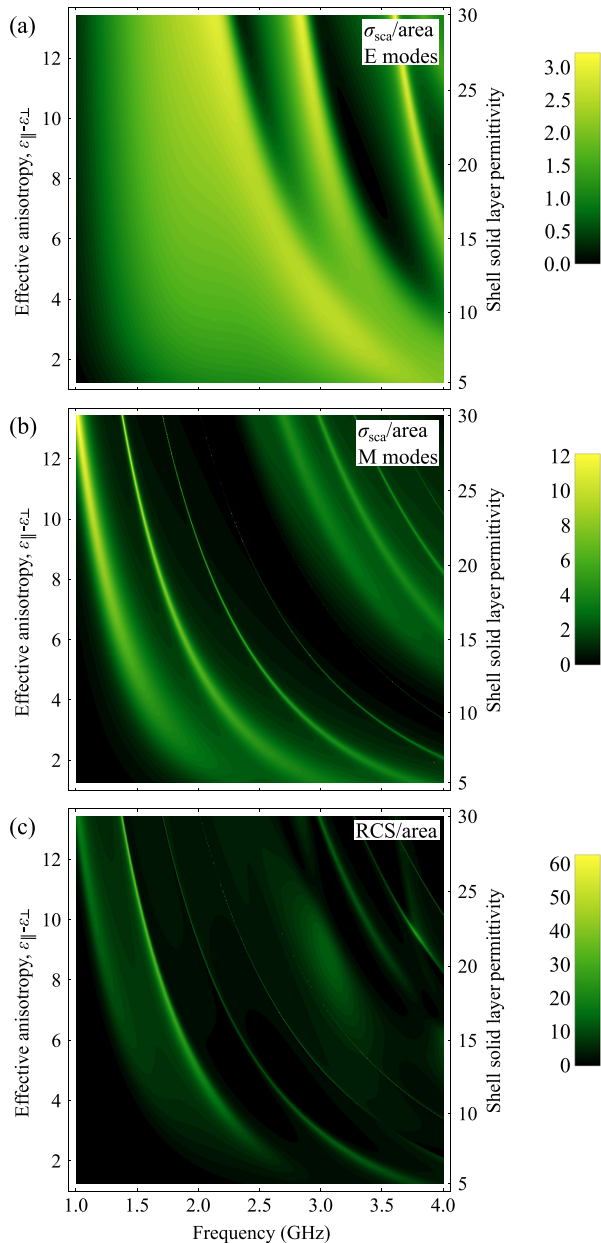


FIG. 5. Analytical Mie theory calculations of scattering for variants of the concentrically layered shell design, in which the relative permittivity of the solid layers of the shell is a variable parameter. The effective anisotropy parameter $\epsilon_{\parallel} - \epsilon_{\perp}$ is shown on the primary ordinate axis. The isotropic permittivity of the solid layers of the shell required to obtain this effective anisotropy is displayed on the secondary ordinate axis. The first five multipoles of each mode family are included. The data are normalized to cross-sectional area. (a) Total scattering cross section contribution due to electric multipoles. (b) Total scattering cross section contribution due to magnetic multipoles. (c) Monostatic RCS.

backscattering of microwave radiation. Analytical theory and numerical method simulations have been used to explain how the spherical structure achieves the enhancement by utilizing radial anisotropy to manipulate its Mie resonances. The demonstration of this mechanism

using a 3D-printed structure adds to the suite of available geometries and concepts for the control of Mie scattering. Through the use of isotropic materials with form anisotropy, the need for anisotropic materials that would require a means of angular alignment in fabrication is avoided. This bio-inspired development has shown the transfer of optical concepts that benefit the visual acuity of the eye of a shrimp to a manufacturable microwave device that has applicability in the manipulation of radar return signals, and can potentially be adapted for other wavelength regimes. The component offers an all-dielectric and partially hollow construction, while providing reflectivity without the requirement for a specific orientation. In this way, the format of the structure is suited to each of the very diverse deployments of the shrimp eye and radar scatterer, while also being capable of assembly using biological processes in optical form as well as fabrication in scaled-up form by additive manufacture for operation at microwave frequencies as demonstrated in this work.

See the supplementary material for additional finite-element simulations of normalized backscatter integrated over the backward hemisphere and total normalized scattering cross section.

This work was funded by the UK Engineering and Physical Sciences Research Council (EPSRC) under Program Grant No. EP/N010493/1: “SYnthesizing 3D METAmaterials for RF, microwave and THz applications” (SYMETA). Alexander Powell would like to acknowledge support from the Royal Academy of Engineering. William Whittow would like to acknowledge support from EPSRC via Grant No. EP/S030301/1: Anisotropic Microwave/Terahertz Metamaterials for Satellite Applications (ANISAT).

AUTHOR DECLARATIONS

Conflict of Interest

The authors have no conflicts to disclose.

Author Contributions

Ewan D. Finlayson: Conceptualization (equal); Data curation (equal); Formal analysis (equal); Investigation (equal); Methodology (equal); Software (equal); Writing – original draft (equal); Writing – review & editing (equal). **Cameron P. Gallagher:** Data curation (equal); Formal analysis (supporting); Investigation (equal); Methodology (equal); Writing – review & editing (equal). **Thomas Whittaker:** Data curation (equal); Formal analysis (supporting); Investigation (equal); Methodology (equal); Writing – review & editing (equal). **Athanasios Goulas:** Data curation (equal); Formal analysis (supporting); Investigation (supporting); Methodology (supporting); Writing – review & editing (equal). **Daniel S. Engström:** Funding acquisition (supporting); Investigation (supporting); Methodology (supporting); Supervision (supporting); Writing – review & editing (equal). **William Whittow:** Conceptualization (supporting); Funding acquisition (lead); Project administration (lead); Supervision (lead); Writing – review & editing (equal). **J. Roy Sambles:** Conceptualization (supporting); Funding acquisition (supporting); Supervision (supporting); Writing – review & editing (equal). **Alastair P. Hibbins:** Conceptualization (supporting); Funding acquisition (supporting); Supervision (supporting); Writing – review & editing (equal).

Alexander W. Powell: Conceptualization (equal); Methodology (equal); Supervision (equal); Writing – review & editing (equal).

DATA AVAILABILITY

The data that support the findings of this study are available from the corresponding authors upon reasonable request.

REFERENCES

- ¹P. Vukusic and J. R. Sambles, *Nature* **424**(6950), 852–855 (2003).
- ²K. Yu, T. Fan, S. Lou, and D. Zhang, *Prog. Mater. Sci.* **58**(6), 825–873 (2013).
- ³C. Pouya, J. T. Overvelde, M. Kolle, J. Aizenberg, K. Bertoldi, J. C. Weaver, and P. Vukusic, *Adv. Opt. Mater.* **4**(1), 99–105 (2016).
- ⁴Y. Kivshar and A. Miroshnichenko, *Opt. Photonics News* **28**(1), 24–31 (2017).
- ⁵Z. Ruan and S. Fan, *Phys. Rev. Lett.* **105**(1), 013901 (2010).
- ⁶A. Ali, M. N. Mohd Yasin, W. F. Faiz Wan Ali, N. Mahmed, M. R. Kamarudin, I. Adam, M. Jusoh, H. A. Rahim, S. F. Khor, and N. Ramli, *Int. J. Antennas Propag.* **2021**, 1–14.
- ⁷A. I. Kuznetsov, A. E. Miroshnichenko, M. L. Brongersma, Y. S. Kivshar, and B. Luk'yanchuk, *Science* **354**(6314), aag2472 (2016).
- ⁸R. E. Jacobsen, A. V. Lavrinenko, and S. Arslanagic, *IEEE Open J. Antennas Propag.* **1**, 493–499 (2020).
- ⁹S. Fakhte and H. Oraizi, *Electron. Lett.* **52**(19), 1579–1580 (2016).
- ¹⁰M. Kerker, D.-S. Wang, and C. Giles, *J. Opt. Soc. Am.* **73**(6), 765–767 (1983).
- ¹¹C. F. Bohren and D. R. Huffman, *Absorption and Scattering of Light by Small Particles* (John Wiley & Sons, 2008).
- ¹²I. Liberal, I. Ederra, R. Gonzalo, and R. W. Ziolkowski, *J. Opt.* **17**(7), 072001 (2015).
- ¹³A. W. Powell, A. P. Hibbins, and J. R. Sambles, *Appl. Phys. Lett.* **118**(25), 251107 (2021).
- ¹⁴K.-L. Wong and H.-T. Chen, *IEE Proc. H (Microwaves, Antennas Propag.)* **139**(4), 314–318 (1992).
- ¹⁵L. Gao, T. Fung, K. Yu, and C. Qiu, *Phys. Rev. E* **78**(4), 046609 (2008).
- ¹⁶B. A. Palmer, A. Hirsch, V. Brumfeld, E. D. Aflalo, I. Pinkas, A. Sagi, S. Rosenne, D. Oron, L. Leiserowitz, and L. Kronik, *Proc. Natl. Acad. Sci. U. S. A.* **115**(10), 2299–2304 (2018).
- ¹⁷B. A. Palmer, V. J. Yallapragada, N. Schiffmann, E. M. Wormser, N. Elad, E. D. Aflalo, A. Sagi, S. Weiner, L. Addadi, and D. Oron, *Nat. Nanotechnol.* **15**(2), 138–144 (2020).
- ¹⁸L. M. Beck, V. J. Yallapragada, A. Upcher, B. A. Palmer, L. Addadi, and D. Oron, *Opt. Express* **29**(13), 20863–20871 (2021).
- ¹⁹A. Machnev, D. Ofer, H. Gilad, J. Binenbaum, L. Schneidman, Y. Levitt-Barmatz, P. Ginzburg, and R. E. Noskov, *ACS Photonics* **10**, 179–184 (2023).
- ²⁰M. Born and E. Wolf, *Principles of Optics*, 6th ed. (Pergamon, New York, 1980).
- ²¹*Comsol Multiphysics*[®], COMSOL AB, Stockholm, Sweden, www.comsol.com (accessed 2023).
- ²²S. Zhang, R. K. Arya, S. Pandey, Y. Vardaxoglou, W. Whittow, and R. Mittra, *IET Microwaves, Antennas Propag.* **10**(13), 1411–1419 (2016).
- ²³D. G. Stavenga, H. L. Leertouwer, D. C. Osorio, and B. D. Wilts, *Light: Sci. Applicat.* **4**(1), e243 (2015).
- ²⁴B. D. Wilts, B. Wijnen, H. L. Leertouwer, U. Steiner, and D. G. Stavenga, *Adv. Opt. Mater.* **5**(3), 1600879 (2017).
- ²⁵A. Goulas, G. Chi-Tangyie, S. Zhang, D. Wang, A. Ketharam, B. Vaidhyanathan, I. M. Reaney, D. A. Cadman, W. Whittow, and J. Y. C. Vardaxoglou, *Ceram. Int.* **47**(6), 7625–7631 (2021).
- ²⁶C. Qian, X. Lin, Y. Yang, X. Xiong, H. Wang, E. Li, I. Kaminer, B. Zhang, and H. Chen, *Phys. Rev. Lett.* **122**(6), 063901 (2019).